Switching dynamics and linear response spectra of a driven one-dimensional nonlinear lattice containing an intrinsic localized mode

M. Sato,[1,*] S. Imai,[1] N. Fujita,[1] W. Shi,[1] Y. Takao,[1] Y. Sada,[1] B. E. Hubbard,[2] B. Ilic,[3] and A. J. Sievers[2]

[1]*Graduate School of Natural Science and Technology, Kanazawa University Kanazawa, Ishikawa 920-1192, Japan*

[2]*Laboratory of Atomic and Solid State Physics, Cornell University Ithaca, New York 14853-2501, USA*

[3]*Cornell Nanoscale Science and Technology Facility, Cornell University Ithaca, New York 14853-2501, USA*

(Received 19 October 2012; revised manuscript received 16 December 2012; published 31 January 2013)

An intrinsic localized mode (ILM) represents a localized vibrational excitation in a nonlinear lattice. Such a mode will stay in resonance as the driver frequency is changed adiabatically until a bifurcation point is reached, at which point the ILM switches and disappears. The dynamics behind switching in such a many body system is examined here through experimental measurements and numerical simulations. Linear response spectra of a driven micromechanical array containing an ILM were measured in the frequency region between two fundamentally different kinds of bifurcation points that separate the large amplitude ILM state from the two low amplitude vibrational states. Just as a natural frequency can be associated with a driven harmonic oscillator, a similar natural frequency has been found for a driven ILM via the beat frequency between it and a weak, tunable probe. This finding has been confirmed using numerical simulations. The behavior of this nonlinear natural frequency plays important but different roles as the two bifurcation points are approached. At the upper transition its frequency coalesces with the driver and the resulting bifurcation is very similar to the saddle-node bifurcation of a single driven Duffing oscillator, which is treated in an Appendix. The lower transition occurs when the four-wave mixing partner of the natural frequency of the ILM intersects the topmost extended band mode of the same symmetry. The properties of linear local modes associated with the driven ILM are also identified experimentally for the first time and numerically but play no role in these transitions.

DOI: 10.1103/PhysRevE.87.012920 PACS number(s): 05.45.−a, 85.85.+j, 63.22.−m, 63.20.Pw

I. INTRODUCTION

A useful advance in the theory of nonlinear excitations in discrete lattices in the late 1980s and early 1990s was the discovery that some localized vibrations in perfectly periodic but nonintegrable lattices can be stabilized by lattice discreteness; that is, the presence of nonlinearity plus discreteness provides a natural habitat for vibrational localization [1–4]. This realization has led to a variety of studies of the features associated with such intrinsic localization [5–8]. In the literature these localized excitations are called either intrinsic localized modes (ILMs) with the emphasis on the fact that they can occur in any dimension and involve no disorder or discrete breathers (DBs) with the emphasis on their similarity to the exact one-dimensional (1D) breather soliton. These unusual modes can occur at any lattice site and may be stationary or move slowly through the lattice. One key element for realistic lattices is the existence of gapped dispersion curves. These nonlinear localized modes have attracted attention both because of fundamental interest [9–18] and also because of possible practical applications [19–28].

A driven 1D micromechanical cantilever array provides a straightforward way in which to examine such localized excitations for systems that have many degrees of freedom [13]. Experimentally, a stationary ILM can be maintained in steady state using a driver to compensate for damping [9,11,29]. Given sufficient starting amplitude it will stay in resonance as the driving frequency is changed adiabatically. In the resultant autoresonant (AR) state the driver frequency controls the ILM amplitude [30–35]. This AR-ILM is stable between two bifurcation frequencies when the driver frequency is the control parameter [22,26]. Only a low amplitude state exists outside this frequency range. With the driver tuned to the topmost frequency of the linear resonance band the excitation pattern changes with increasing driver frequency as follows: a uniform excitation pattern of the top mode of the band, chaotic moving ILMs, a low amplitude state, the AR-ILM state of interest, and finally a low amplitude state. The AR state is achieved only when the driver frequency is chirped up with sufficient speed from the top of the band frequency to pass the low energy state separating the linear resonance frequency regime from the AR state, which is bounded by the upper bifurcation point. When the driver frequency is decreased from inside the AR state, the ILM disappears into a low amplitude state at the lower bifurcation frequency. As yet the properties and dynamics of ILMs near the bifurcation points have only been described in a brief report [26].

Although the ILM's shape changes with the driver frequency, one of the switching results for such a driven many body system seems intriguingly similar to that previously observed for the transition of a Duffing oscillator in the AR state (a single degree of freedom). Studies of a single driven nonlinear oscillator that obeys the Duffing equation have a long history and reveal a variety of phenomena from a linearlike resonance to chaos [36], depending on the driving condition. The most well known effect is hysteresis that accompanies a sudden change of amplitude when the driver is swept up or down over a certain frequency range. Because the Duffing resonator is the simplest nonlinear oscillator with these phenomena, this model system has been used for a variety of theoretical studies [37–41], for developing new ideas [31,42], and for applications [43–45]. A stochastic resonance when the Duffing resonator is at a kinetic phase transition, where

*msato@kenroku.kanazawa-u.ac.jp

the system is simultaneously in 50% high and 50% low amplitude states, is one example [46,47]. Another example is a bifurcation amplifier, which uses the sudden change at the bifurcation to amplify a signal [43].

Prediction of the bifurcation point for a single nonlinear Duffing oscillator has been studied in some detail since such a catastrophic change in oscillator behavior is important from an applications point of view. To forecast a sudden rise of a vibration amplitude of a single driven Duffing resonator from a low amplitude state [36,48], a beat frequency between a driver and a phase mode was observed to decrease when the bifurcation point was approached. A natural question to ask is how similar is the many body AR-ILM bifurcation property to that of the single AR oscillator? A related question is how different could it be?

The spectrum of local modes associated with a large amplitude ILM have now been examined in some detail. A variety of linear resonances have been observed and interpreted. They include the natural frequency [NF] of the ILM, this NF is for an ILM with the same amplitude pattern but no driver nor damping. Even and Odd linear localized modes (LLMs) [15,49] are also present. What role, if any, do these resonances play in the bifurcation transition?

In order to determine how similar the dynamics of the upper bifurcation point of the ILM is to the single Duffing oscillator result, the next section of this paper focuses on the large amplitude behavior and the NF property of a driven damped Duffing resonator. To see this linear mode a second variable frequency driver called a probe is introduced so that the NF can be observed in the presence of damping. The NF peak and its four-wave partner (NF) appear as distinct structures in the response spectrum. Section III describes the experimental setup for the ILM study in a 1D micromechanical cantilever array. The probe is very weak with respect to the driver locked to the ILM, and hence does not perturb the ILM, but is still strong enough to see linear localized features produced by it. The experimental probe spectra results are presented in Sec. IV. A variety of linear resonances have been observed and interpreted. They include the NF of the ILM, an even LLM [15,49] of the ILM, and also the topmost extended band modes. The simulations, described in Sec. V, are used to confirm the sources of some of the resonant features near the bifurcation points. Section VI considers the resemblance between the driven ILM and the single driven Duffing resonator at the upper bifurcation point and described the more complex behavior at the lower bifurcation point. By examining their different behaviors near the bifurcation points, experimentally and through numerical simulations, and by comparing the results with those found for a single Duffing oscillator, the bifurcation dynamics of ILMs have been quantitatively characterized. Some possible applications of linear probe spectroscopy to nonlinear systems are also discussed. The conclusions emphasize the importance of the NF role to understanding the bifurcation dynamics. An appendix quantifying the analytical NF spectrum results of the singe Duffing resonator follows.

II. BACKGROUND

Since the NF of the ILM will play an important role in the understanding of its bifurcation transitions, first we describe how one can observe the NF of the simplest nonlinear system, namely, the single Duffing resonator. It is well known that the general solution for a driven harmonic oscillator with NF $= \omega_0$ and driver frequency Ω and no damping is the sum of two contributions [50]. One is the general solution of the homogeneous equation while the other is a particular integral of the inhomogeneous equation. For the case of small oscillations near the NF ω_0 the resulting signature appears in the form of beats with frequency $\omega_b = |\omega_0 - \Omega|$. As the driver approaches NF the beat frequency goes to zero, $\omega_b \to 0$, a transition to the resonant state occurs, and the small signal method is no longer valid. When damping is included and the driven oscillator inspected after a sufficiently long time only the particular solution of the inhomogeneous equation with driver frequency Ω remains in this steady state. To recover the beat signal a second (weak) source with tunable frequency ω, usually called the probe, is introduced. The maximum amplitude for the beat now occurs when $\omega = \omega_0$, giving the same NF condition as before. Once again, as the driver and NF approach each other the amplitude at the NF grows.

The corresponding NF of a nonlinear oscillator can be identified in terms of its asymptotic limit as the driver and damping simultaneously go to zero (so that its amplitude remains fixed), then the resonance plays the same role as the NF for a driven harmonic oscillator without damping. To be more quantitative consider the single Duffing oscillator given by

$$\ddot{x} + \frac{1}{\tau}\dot{x} + \omega_0^2 x + \varepsilon x^3 = \alpha_d \cos\Omega t + \alpha_p \cos\omega t, \qquad (1)$$

where τ is the relaxation time, ω_0^2 is square of the linear resonance frequency, $\epsilon > 0$ is a hard nonlinear constant, α_d and α_p are the acceleration amplitudes for the driver and probe, and Ω and ω are the driver and probe frequencies, respectively. A high amplitude state of the Duffing oscillator is obtained by driving it at a frequency Ω slightly above ω_0. Next, with the driver frequency fixed, a weak probe oscillator is initiated at a frequency nearby, where $\omega \sim \Omega$. The analytical form for the amplitude response curve can be obtained by assuming the displacement has three frequency components so that

$$x = \tfrac{1}{2}\tilde{A}e^{-i\Omega t} + \tfrac{1}{2}\tilde{a}e^{-i\omega t} + \tfrac{1}{2}\tilde{b}e^{-i\omega' t} + \text{c.c.} \qquad (2)$$

Here $\omega' = 2\Omega - \omega$ is the four-wave mixing frequency, $\tilde{A}$ is the large oscillation driver response, $\tilde{a}$ is the probe response, and $\tilde{b}$ is the four-component response. [The term four-wave mixing is used in analogy with optics terminology to describe the nonlinear process generated by the cubic term in Eq. (1).] Weak vibration components, such as that at $2\omega - \Omega$, proportional to $|\tilde{a}|^2\tilde{A}$, are omitted because they are much smaller than those that vary like $|\tilde{A}|^2\tilde{a}$ vibrating at $\omega' = 2\Omega - \omega$. The probe response function $\tilde{\chi}(\omega)$ can be calculated from Eq. (2):

$$\text{Re}[\tilde{\chi}(\omega)e^{-i\omega t}] = \text{Re}[\tilde{a}/\alpha_p]\cos\omega t + \text{Im}[\tilde{a}/\alpha_p]\sin\omega t. \qquad (3)$$

The details of the probe response function calculation for this Duffing oscillator, which results in four resonances, are given in the Appendix. As mentioned there, the response function can also be calculated as a fluctuation spectrum [46,51]. As to be expected from the fluctuation-dissipation theorem the response function and the fluctuation spectrum give the same information.

From Eq. (A3) in the Appendix the response function resonances are at

$$\omega_n = \Omega \pm \sqrt{\Omega^2 + \omega_{nl}^2 \pm \sqrt{4\Omega^2\omega_{nl}^2 + \left(\tfrac{3}{4}\varepsilon|\tilde{A}|^2\right)^2}}, \qquad (4)$$

where the bare nonlinear NF is $\omega_{nl}^2 = \omega_0^2 + \frac{3}{2}\varepsilon|\tilde{A}|^2$. The positive sign under the radical in Eq. (4) gives two solutions far from the driver frequency at $\omega \approx -\Omega$ and 3Ω. The solutions of interest are those near the driver frequency Ω and equidistant from it. The imaginary part of this response function has a positive peak above the driver frequency and a negative peak symmetrically placed below it at a high amplitude state. The negative peak becomes comparable in amplitude to the positive one when the oscillating amplitude $|\tilde{A}|$ is large. As expected, as $|\tilde{A}| \to 0$, the positive peak approaches the linear NF ω_0, and the negative response peak disappears. For these two symmetrical resonances about the driver, the upper one is the nonlinear NF because of its remaining activity as $|\tilde{A}| \to 0$ and because of its positive sign, while the lower negative one is its nonlinear mixing partner from the cubic term in Eq. (1) because of its disappearance as $|\tilde{A}| \to 0$. If either resonance is driven by the probe oscillator, the other sideband is generated by nonlinear mixing.

Figure 1 provides a general overview of the probe response for the Duffing oscillator both in and out of the AR states. The parameters used are similar to those that apply to measurements associated with the AR-ILM state. Figure 1(a) is the familiar amplitude versus frequency curves. When the driver frequency is decreased from above the previous bifurcation frequency toward the linear resonance frequency the amplitude can suddenly jump from a low to a large value. This is the case studied in Ref. [48]. The results are also presented by Thompson and Stewart [36]. The imaginary part of probe response curves for driver frequencies "A," "B," and "C" in Fig. 1(b) correspond to these cases. Note that the NF is lower than the driver frequency. The bifurcation takes place when the beat frequency goes to zero so that the nonlinear NF is suddenly in resonance. After the bifurcation, the positive peak for the NF appears above the driver while a negative peak is observed below, as shown in the curve "D" of Fig. 1(b). This is caused by the nonlinear mixing between the driver and the NF. When the driver frequency is decreased further, only the NF positive peak appears at the linear resonance frequency ω_0.

Conversely, when the driver frequency increases from "F" to above the linear resonance frequency ω_0, the amplitude increases until the driver frequency reaches a bifurcation frequency "H" where the amplitude drops suddenly to a small value. Here, we describe the sudden drop at the high frequency bifurcation point in terms of the NF. In the AR state the NF $= \omega_n$ is slightly larger than the driver frequency. Note that the positive peaks in the curves "F" to "H" are all higher than the driver frequency. As the driver frequency increases, the NF increases but at a slower rate so that the beat frequency decreases. At the bifurcation point, $\omega_n - \Omega = 0$ and the amplitude of the NF frequency resonance takes its maximum value. Its phase is shifted by $-90°$; the same behavior as observed for a damped, linear resonator. Beyond this point the oscillator uncouples from the driver, and the amplitude drops suddenly.

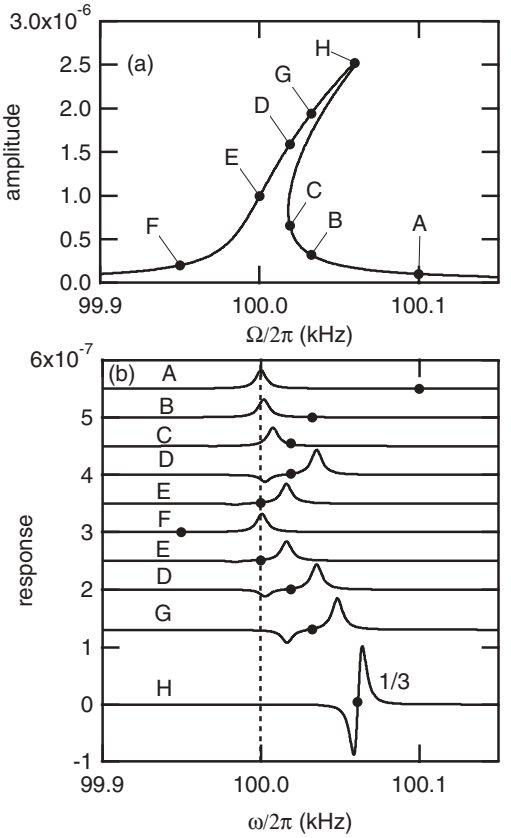

FIG. 1. (a) The Duffing resonator amplitude as a function of the driver frequency $\Omega/2\pi$. (b) Imaginary part of the linear response curve at driver frequencies indicated by letters in (a). The vertical dashed line indicates the linear resonance frequency $\omega_0/2\pi$. Solid circles indicate the driver frequency for each spectrum. When the vibration amplitude is low, as in case "A," the response curve has one peak at the dashed line. When the driver frequency decreases from "A," its amplitude suddenly jumps at the bifurcation point "C." During this approach, the peak shifts toward the driver frequency. After the bifurcation "D," there are two peaks: One is positive above the driver and the other is negative and below the driver. As the driver frequency decreases further, "E," the negative peak becomes smaller. When the driver frequency is very low, as in "F," there is only one positive peak at the linear resonance frequency. When the driver frequency increases from "F" to "H," the positive peak is always above the driver frequency until the driver reaches to the other bifurcation, "H." The difference frequency between the positive peak and the driver frequency becomes small and the peak height diverges at the bifurcation point "H." The curve for "H" is reduced to 1/3. Parameters are $\omega_0/2\pi = 100$ kHz, $\epsilon = 1 \times 10^{20}$ $(1/\mathrm{m}^2\mathrm{s}^2)$, $\tau = 0.02$ (s) and $\alpha_d = 80$ $(\mathrm{m}/\mathrm{s}^2)$.

Another point of view considers the sidebands as Stokes and anti-Stokes lines [51]. However, for this lattice system, some positive peaks appear below the driver frequency in the spectra because of the many degrees of freedom, as we will see below. Thus, identifying them in terms of the sign of the imaginary response is more relevant than signifying them in terms of their relative frequency position with respect to the driver. By distinguishing the positive peaks as resonances all the important resonant modes, including extended band modes can be identified for the lattice system. These features can be

continued down to smaller amplitudes where positive response is found for the linear state. From this perspective, all negative peaks are four-wave mixing (cubic in the equation of motion) partners of corresponding positive ones.

These two oppositely directed amplitude transitions are often described as saddle-node bifurcations. When approaching such a bifurcation point by changing the driver frequency, an unstable solution approaches the stable solution; hence, the decrease in the beat frequency is the signal of an approaching unstable solution. The van der Pol plane [52] is a suitable way to consider the large amplitude driver response and the small amplitude NF in phase space, because this frame rotates with the driver frequency. Figure 2(a) shows a typical phase plane

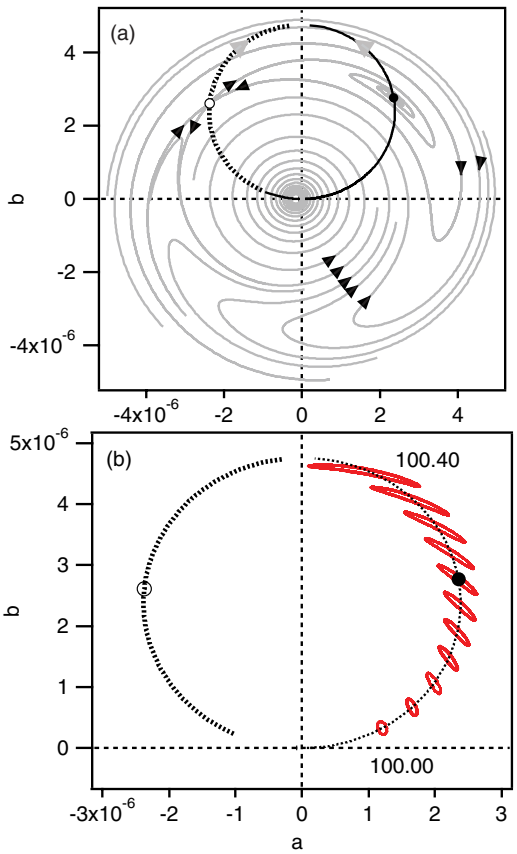

FIG. 2. (Color online) (a) Paths in the van der Pol phase plane of the Duffing oscillator. Gray curves indicate paths at a fixed driver frequency. The distance from the origin to the open and closed circles show the amplitudes for the unstable (saddle) and high amplitude stable (node) fixed points. A low amplitude stable point is near the origin. Solid and dashed curves with gray arrows illustrate movement of the high amplitude stable point and unstable point with increasing driver frequency and merge at the top of this figure where saddle-node bifurcation takes place. (b) An ellipse represents the amplitude path of the driven excitation when the NF is excited by a weak probe. A series of magnified elliptical paths are shown, each around the appropriate stable point for a specific driver frequency. The driver frequency is increased from 100 to 100.4 kHz in 40-Hz steps. Open and solid circles are the unstable point and stable point in panel (a) for a 100.24-kHz driver frequency. As the saddle-node bifurcation is approached, the aspect ratio of the ellipse grows. Parameters in Eq. (1) are $\omega_0 = 10^5 \times 2\pi$ s^{-1}, $\tau = 0.01$ s, $\epsilon = 1.97 \times 10^{20}$ s^{-2} m^{-2}, $\alpha_d = 300$ m/s^2, $\alpha_p = 5$ m/s^2, and $\Omega = 1.000$ to $1.040 \times 10^5 \times 2\pi$ s^{-1}.

for the large amplitude driver response of a Duffing resonator. It shows three fixed points: a stable high amplitude node represented by the distance from the origin to the solid dot, a stable low amplitude node near the origin, and an unstable saddle point. The high amplitude node and unstable saddle approach each other at the top of this figure with increasing driver frequency; the result is pair annihilation at the bifurcation point. An elliptical curve in Fig. 2(b) describes the orbit of the large amplitude driver response, when it is perturbed by the probe at the nearby NF frequency. The (period)$^{-1}$ is the difference frequency between NF and the driver, i.e., the beat frequency. The orbit shape is elliptic due to the local dynamic property around the fixed point. In Fig. 2(b), a relatively large probe perturbation is applied to magnify the effect; however, the perturbation actually is very small so that a linear response function $\chi(\omega)$ applies. The approach of the unstable solution modifies the local environment around the stable point. Since an orbit near the saddle moves slowly, the rotation period of the ellipse becomes longer when the driver frequency is closer to the bifurcation point, i.e., the beat frequency decreases. Thus, the NF intersecting the driver in frequency space and the saddle-node bifurcation picture in the van der Pol phase space provide complementary views of same transition.

III. EXPERIMENTAL SETUP

With the pump-probe experiments described here the properties of a driven ILM near its bifurcation points have been measured. Figure 3(a) shows the experimental setup. The

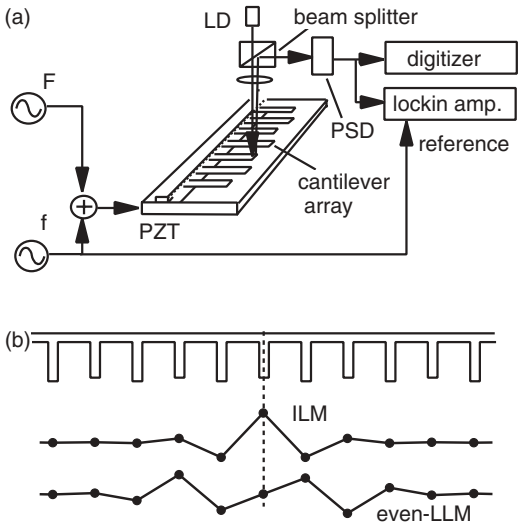

FIG. 3. (a) Experimental setup for the linear response measurement of the AR state by the uniform probe perturbation. The array is composed of alternating 50- and 55-μm-length cantilevers. The driver at frequency F and probe signal at frequency f are added and used to excite the array uniformly by the thin piezoelectric transducer (PZT). A laser diode (LD) illuminates a cantilever nearby the ILM and the reflected beam is detected by a position sensitive detector (PSD). The displacement signal is recorded by a digitizer or, analyzed by a lock-in amplifier. A typical driver amplitude is 14 V, while the probe amplitude is 12 mV. (b) Spatial pattern of a large amplitude ILM and a small amplitude (magnified) even mode LLM at a particular cantilever site.

driven micromechanical array contains 152 cantilevers coupled together by a common overhang. Because of the positive nonlinearity of the cantilever array, the ILM is generated above the top of the linear dispersion curve. We designed a dielement array so that it is possible to excite the highest frequency normal plane wave mode with a uniform driver. Uniform excitation is achieved easily by shaking the entire sample up and down with a piezoelectric transducer (PZT) attached to the sample bottom. Because of the mass difference between the short and long cantilevers in a unit cell uniform acceleration produces a different force on each. A cw driver oscillator with frequency F feeds energy to the array maintaining the ILM in the large amplitude AR state. For linear response measurements an additional weak probe oscillator with frequency f is used to perturb the array. The output of the probe oscillator is combined with the strong driver and connected to the PZT so the perturbation is applied uniformly across the lattice. With an ILM present the motion of a nearby single cantilever is monitored using a diode laser and a position sensitive detector (PSD, Hamamatsu Photonics). A lock-in amplifier or a digitizer is used to selectively analyze the cantilever motion that is caused by the probe oscillating at a given frequency. A response spectrum is measured by scanning the probe frequency, while the driver frequency is held fixed. By then changing the driver frequency in a stepwise fashion, the linear mode properties can be monitored as a bifurcation point is approached.

With fixed boundary conditions, or via symmetry breaking by the AR ILM state, all linear modes can be classified into odd and even symmetries in terms of the vibrating spatial pattern and appear alternatively when ordered by their mode frequency. For example, the ILM shown in Fig. 3(b) is odd and the LLM (in Ref. [15]) is even. In the absence of impurities our method measures only odd modes, i.e., a vibration pattern $(\ldots, -0.4, 1, -0.4, \ldots)$ that has a finite coupling to the uniform acceleration driver with the dielement mass pattern. Even modes are not recorded in these spectra; however, if impurities exist to one side of the ILM, the broken symmetry makes the local even mode observable.

Observing a small probe signal near the frequency of the ILM, which produces about 1000 times larger signal, is a problem. In addition, any perturbation could cause a drastic change in the vibration spectrum, such as broadband chaotic noise, since the ILM is a nonlinear phenomenon. For these reasons, we first examined the FFT spectrum from the digitizer (12 bit) of the PSD signal. Because of the limited bit width of the digitizer, we used a slightly larger probe amplitude for this case. The FFT spectrum of the ILM at a fixed probe frequency f and driver frequency F is shown in Fig. 4(a). The large peak at the center is the ILM vibration at the driver frequency. The center peak height is normalized to 1 and the ordinate is magnified to see the weak structure produced by the probe perturbation. The upper frequency narrow peak is the response of the probe. There is another peak symmetric to the driver on the lower frequency side, which is the four-wave mixing signal at $2F - f$. By changing the probe frequency in a stepwise fashion, we obtain the spectral map as shown in Fig. 4(b). The two crossing patterns connecting opposite corners identify $f_{\mathrm{FFT}} = f$ and $f_{\mathrm{FFT}} = 2F - f$, and they are due to the probe response signal and four-wave mixing signal, respectively. There are no other signals except the ILM. Figure 4(c) shows

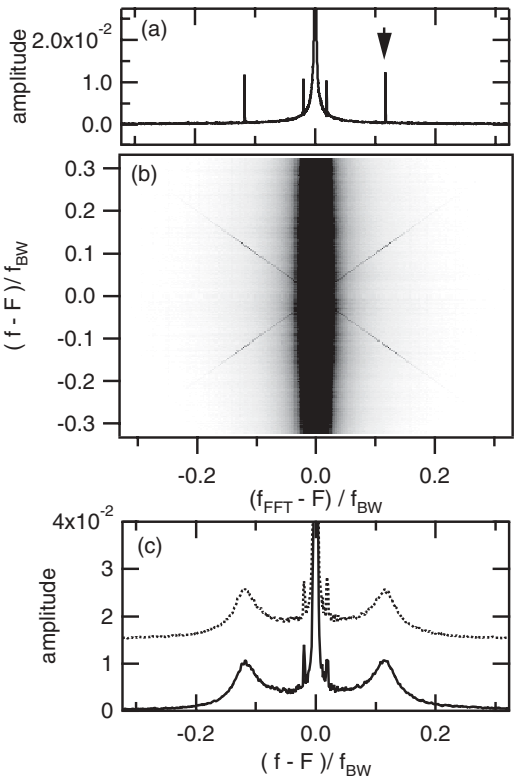

FIG. 4. (a) The ILM vibration spectra by FFT. Abscissa is the difference frequency of the FFT frequency and the driver frequency normalized by the bandwidth of the linear normal mode. The center peak is the ILM. The spectrum is normalized by its peak height and magnified to see the small structures. The probe perturbation is applied at a frequency indicated by the arrow. There is four-wave mixing signal at opposite side of the center peak. Two other peaks nearby the center are spurious from the driver oscillator. (b) A probe response map made from step scanned FFT spectra. Abscissa is the driver-difference FFT frequency, and the ordinate is the driver-difference probe frequency. The probe frequency is changed stepwise, and an FFT spectrum is obtained at each step. This figure is made from 500 FFT spectra. The dark vertical center structure is the ILM signal at the driver frequency. There are signals on two lines crossing at the center. The signal on $f_{\mathrm{FFT}} = f$ is the probe response signal, and the signal on the other straight line $f_{\mathrm{FFT}} = 2F - f$ is by the four-wave mixing. (c) Probe response spectrum (solid line) and four-wave mixing signal (dashed line) as a function of the probe frequency. These are calculated from the map.

the spectra deduced from the map of the signals on the crossing lines. Two broad resonance structures are seen: The upper one is the NF and the lower one is its nonlinear mixing partner.

Figures 4(b) and 4(c) demonstrate that the probe causes a small perturbation producing only two clean signals. The signal on the line $f_{\mathrm{FFT}} = f$ is the probe response spectrum. More importantly, Figs. 4(a)–4(c) show that the broad resonant structure in Fig. 4(c) is not due to the spectral width of the driving oscillators used in these experiments or by some nonlinear process, but due to a real feature that should be assigned to the NF resonance. Hereafter, a lock-in amplifier (ITHACO-NF 3961B) was used instead of the digitizer and the measured signal at the probe frequency was obtained with a combination of two digital multimeters connected to the cosine

and sine outputs. The internal AD converters of the lock-in amplifier cannot be used, because a small gain setting of the amplifier is required to avoid saturation by the ILM signal, and because the probe signal is too small for the internal AD converters at such settings. However, measurements with the external multimeters presents no problem since their ranges can be set independently. A probe spectrum was taken at a fixed driver frequency. We compared spectra taken by these two methods and made sure that the lock-in amplifier method produced the same spectrum, then reduced the probe driver amplitude to a small value consistent with a good signal to noise ratio. The driver frequency is changed stepwise, and this process is repeated over the entire AR state.

IV. EXPERIMENTAL RESULTS

The AR ILM amplitude as a function of the driver frequency F is shown in Fig. 5. The amplitude was measured using the setup in Fig. 3(a), with the reference signal of the lock-in amplifier connected to the driver. Generation of an ILM is made by chirping up the driver frequency from the top of the optic band to the middle of the AR region. Because of the irreversible nature of the AR state beyond the transition points, a measurement sequence is initiated from the middle frequency region (open circle), and the driver frequency is then step incremented slowly up or down. The lower abscissa in Fig. 5 is the driver frequency normalized to the top of the linear optic band frequency. The upper abscissa is the difference frequency between the driver F and the linear optic mode frequency f_T normalized by the optical bandwidth f_{BW}. (This ratio provides a general measure of the strength of the nonlinearity for this driven system.)

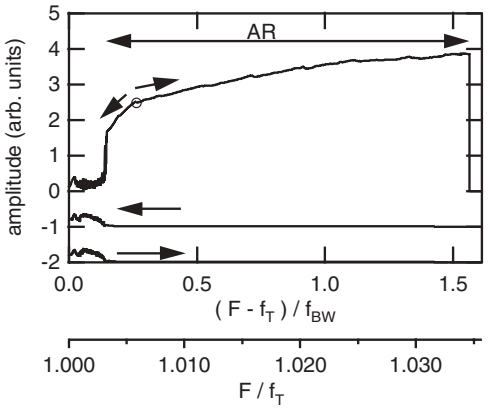

FIG. 5. Experimentally observed AR amplitude as a function of the driver frequency F. Lower abscissa: driver frequency normalized to the top of the optic branch. Upper abscissa: difference frequency between the driver and the top of the optic branch ($f_T = 140.0$ kHz) normalized by the band width (3.1 kHz). The stable AR region indicated by "AR" is 140.46 to 144.85 kHz, or 0.148 to 1.57 by the normalized difference frequency. First, the AR-ILM was generated by rapidly chirping up the driver frequency from top of the band. Open circle indicates the end frequency of the chirping, and it is starting point of the measurement. From this point, the driver frequency was either scanned down or scanned up. Lower two curves are the results for scanning down or up from outside of the AR state. The noisy amplitude in the low frequency region is due to chaotic traveling ILMs. Curves are shifted for clarity.

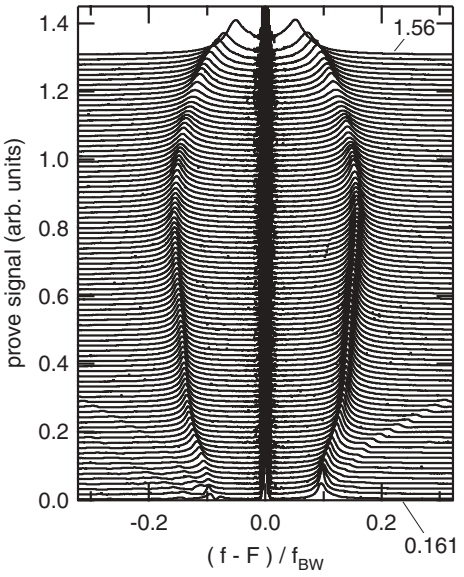

FIG. 6. Experimental response spectra for the AR state as a function of the normalized difference frequency. The gap frequency of the large sideband peaks (beat frequency) decreases and the response grows as the driver frequency approaches the upper bifurcation point. Observed sidebands are produced by a NF of the ILM oscillation. Spectra are aligned from 140.5 to 144.85 kHz with 50-Hz steps from bottom to top [0.161 to 1.56 by the normalized difference frequency $(F - f_T)/f_{\mathrm{BW}}$]. The upper and lower frequency limits are near the two bifurcation frequencies. The abscissa is normalized by the bandwidth of the optic branch.

To reach the high amplitude state the driver frequency must increase at a sufficient rate to cross over from the low amplitude state, through the chaotic state, to the AR state [53]. With a slow scan of the driver frequency, the AR state cannot be reached, as shown by the bottom trace in Fig. 5. The middle trace is the result of scanning down from above the upper bifurcation frequency, showing that the AR state is a metastable state.

The measured linear response spectra for the AR state at different driver frequencies are presented in Fig. 6, which show resonance peaks near the driver frequency and also extended band modes. Movement of the resonance peaks toward the upper or lower bifurcation points provide dynamical evidence for the bifurcation mechanisms. The two strong sidebands shown in Fig. 6 are due to the NF of the AR state. (See simulations in Sec. V for confirmation.) The probe spectra are displayed with the driver frequency varying from 140.50 to 144.85 kHz in 50-Hz intervals from bottom to top. This range corresponds to 0.161–1.56 in terms of the difference frequency normalized by the bandwidth. The higher frequency sideband is the NF while the lower frequency one is its four-wave mixing partner. The two driver frequency limits shown are close to the upper and lower bifurcation frequencies, and so the frequency range essentially corresponds to the entire stable region of the AR state. Note that the difference frequency of the sidebands to the driver (the beat frequency) decreases and the response grows as the driver frequency approaches the upper bifurcation point. One of the weak satellite features that appears near the low frequency transition is an extended wave in the optic branch.

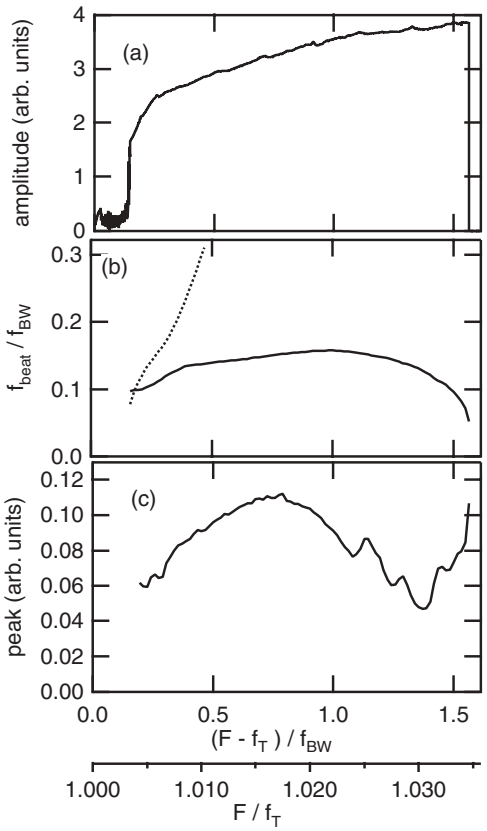

FIG. 7. (a) AR amplitude of the ILM as a function of the driver frequency. (b) The NF (solid) and the even LLM (dashed) beat frequencies as a function of the driver frequency. The data show that the NF approaches the driver frequency at the upper bifurcation point while the LLM frequency does not. (c) NF peak height as a function of the driver frequency. It diverges at the upper bifurcaiton point. The peak height does not increase monotonically over part of the region due to an experimental problem giving a lower sensitivity of the probe amplitude at the larger ILM condition.

The NF beat frequency and its peak height are summarized in Figs. 7(a) and 7(c) for the AR amplitude as a function of the driver frequency shown in Fig. 7(a). The beat frequency (solid) first increases, then decreases as the upper bifurcation point is approached, as shown in Fig. 7(b). The resonance amplitude first increases with driver frequency, next decreases, and finally increases rapidly as the upper bifurcation point is approached. The decrease in the middle region may be due to an experimental error because of the large oscillation amplitude of the ILM and because of suppressed gain of the middle stage of the equipment affected by the large ILM signal. From this figure, it is clear that the beat frequency decreases and the amplitude diverges as the upper bifurcation point is approached. On the other hand, there is no similar signature with regard to the bifurcation mechanism for the lower bifurcation point in this figure.

By plotting the imaginary part of the linear response spectrum as a function of the probe frequency for fixed driver in Fig. 8, the results can be used to explore the lower bifurcation point. The large symmetrically located positive and negative peaks are due to the NF and its mixing partner. There are several small resonant structures below its lower sideband

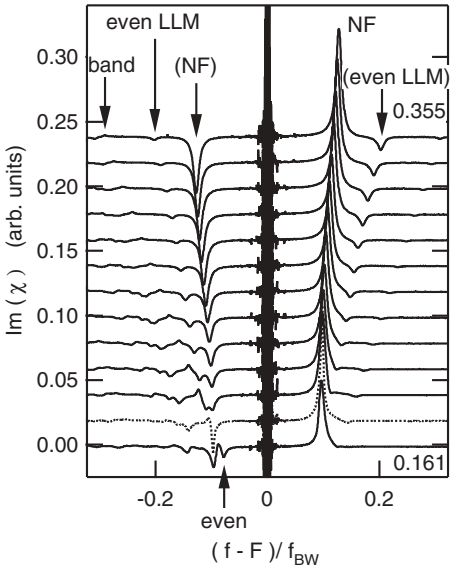

FIG. 8. Experimental imaginary part of the response as a function of the normalized difference probe frequency. Spectra near by the lower bifurcation are ordered by the driver frequency from 0.355 to 0.161 in 0.016 steps. The large peak at the center is the ILM signal. "NF" denotes natural frequency peak, and letters inside parentheses are for their four-wave mixing partners. The lower bifurcation takes place at 0.148. The even LLM is identified between the band mode and the lower (NF). It is activated weakly by an asymmetry caused by the probe laser heating or an impurity. The even LLM crosses with the lower NF. Band modes are seen as a sequence of small peaks and the label "band" is placed at the highest frequency mode. The lower bifurcation takes place when the lower (NF) coalesces with the band mode.

peak. As the lower bifurcation point is approached, one of them crosses the lower sideband peak of the NF. By comparison with simulations (below), we identify this mode as an even-LLM, while the other mode, relatively far from the lower NF, is an extended band mode. The even mode is not activated by the uniform driver so it cannot be measured normally with this technique; however, it may be activated by an impurity or imperfection. The probe laser can be a source of such an impurity, since it is sharply focused to one side of the ILM. The dashed curve in Fig. 7(b) shows the driver frequency dependence of the even LLM. From experiments shown in Fig. 8 the lower bifurcation takes place when the (NF) reaches the band mode.

V. SIMULATIONS

A lumped element model of the cantilever array is used for simulations with equations of motion of the form

$$\begin{aligned} m_i \frac{d^2x_i}{dt^2} + \frac{m_i}{\tau}\frac{dx_i}{dt} + k_{2Oi}x_i + k_{4O}x_i^3 \\ + \sum_j k_{2I}^{(j)}(2x_i - x_{i+j} - x_{i-j}) \\ + k_{4I}\{(x_i - x_{i+1})^3 + (x_i - x_{i-1})^3\} \\ = m_i\alpha_d \cos\Omega t + m_i\alpha_p \cos\omega t, \end{aligned} \tag{5}$$

where i is the site number of the cantilever, m_i is the mass, τ is the relaxation time, k_{2Oi} and k_{4O} are harmonic and quartic

TABLE I. Parameters used in simulations. Values are the same as in Ref. [24].

Symbol	m_i (kg)[a]	k_{2Oi} (N/m)[a]	$k_{2I}^{(j)}$ (N/m)[b]	τ (s)	k_{4O} (N/m^3)	k_{4I} (N/m^3)
Value	7.67×10^{-13}	0.142 277	0.082 845 3	8.75×10^{-3}	1.0×10^{8}	4.0×10^{10}
	6.98×10^{-13}	0.168 389	0.030 8231			
			0.010 831			
			0.004 047 21			
			0.002 495 21			
			0.000 823 741			

[a]The upper row is for the longer cantilever; the lower row is for the shorter cantilever.
[b]Listed from nearest neighbor to sixth nearest.

onsite spring constant, $k_{2I}^{(j)}$ is the harmonic spring constant for the intersite connection up to sixth neighbor, and k_{4I} is the quartic spring constant for the intersite connection. The right hand side is the driving term. Here to match experiment $\alpha_d = 1000$ m/s^2 is the driver acceleration and Ω is the driver frequency. The second term is for the probe at frequency ω and acceleration amplitude $\alpha_p = 0.01$ m/s^2. Fixed boundary conditions are used and the total number of cantilevers is 100. The specific lattice parameters, listed in Table I, are determined by experimental observation and comparison with simulations.

Figure 9(a) shows the calculated amplitude of the AR-ILM as a function of the driver frequency. It is obtained by decreasing or increasing the driver frequency from the middle of the AR-ILM frequency region. Below the lower bifurcation frequency exists the low amplitude, no ILM state. On the other hand, Fig. 9(b) presents results of simulation starting from the no ILM, low amplitude state while changing the driver frequency either up or down. The AR-ILM state is achieved only when the driver frequency is chirped up rapidly to pass through the low amplitude state. At a slow speed of scanning, the end result is no ILM as shown by bottom traces in Fig. 9(b). When the driver frequency decreases from above the upper bifurcation frequency, the low amplitude state is maintained through the AR frequency region. The small amplitude at the bottom curve in Fig. 9(b) illustrates where chaotic traveling ILMs can be realized.

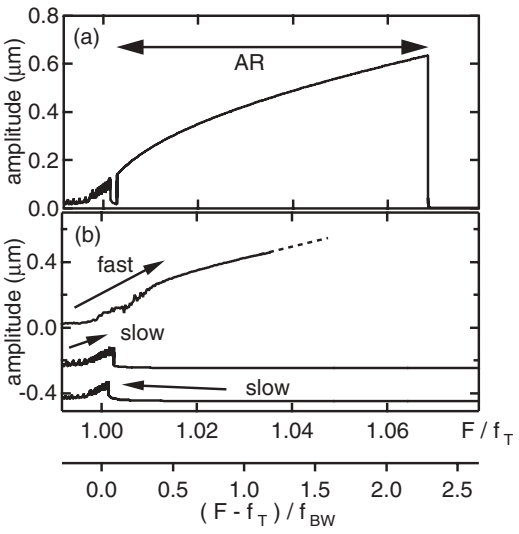

FIG. 9. (a) Simulated AR-ILM amplitude as a function of the driver frequency with driver appropriate to the experimental level. The AR region is identified between two transitions at edges. The stable frequency region is 137.56 to 146.54 kHz, or 0.102 to 2.29 by the normalized difference frequency. (b) Amplitude vs driver frequency for different chirping or starting conditions. Top trace, fast frequency rate required to reach the AR-ILM state. Bottom two traces, slow up and down scanning; no AR state occurs. The top of the band frequency is 137.14 kHz and the band width is 4.1 kHz. Curves are shifted down for clarity.

The calculation of the response spectrum is carried out in a manner similar to the experiments. First, the ILM is generated. Then, the uniform probe is applied. Displacement at the center site of the ILM is multiplied by cosine and sine functions vibrating with the probe frequency. Two set of simulations with opposite phases of the probe driver are made, then by subtracting one from the other the large oscillation component produced by the ILM can be eliminated. The long time average of the cosine and sine multiplied displacements gives the real and imaginary parts of response functions and then by changing the probe frequency slowly, the response spectra are calculated.

Figure 10 presents the magnitude of the linear response spectra as a function of the normalized beat frequency between the driver and the probe. The traces are for different driver frequencies throughout the entire stable AR region. As the upper bifurcation point is approached at the top of the figure, the two symmetric peaks, the NF and its mixing partner, move toward the driver frequency, at the center, and their amplitudes increase. As the lower bifurcation point is approached at the bottom of the figure the mixing partner of the NF moves toward and finally intersects the topmost band mode of the array. The band modes are magnified by 20-fold to make them visible on this plot.

The driver frequency dependencies of two different kinds of beats are shown in Fig. 11. In these plots the abscissa presents the driver frequency with respect to the top of the band mode spectrum normalized by the bandwidth of the optic branch. This provides a normalized measure of the nonlinearity. In Fig. 11(a) the amplitude of the center of the ILM for two different driving accelerations, $\alpha_d = 300$ m/s^2 and $\alpha_d = 1000$ m/s^2, are displayed, defining the corresponding AR state. In Fig. 11(b) the normalized beat frequency of the NF (solid line) and LLM (dashed line) are shown for $\alpha_d = 1000$ m/s^2. Note that the NF beat decreases as the upper bifurcation is approached. The peak height displayed in Fig. 11(c) diverges as the beat frequency decreases. [Also note there is a small

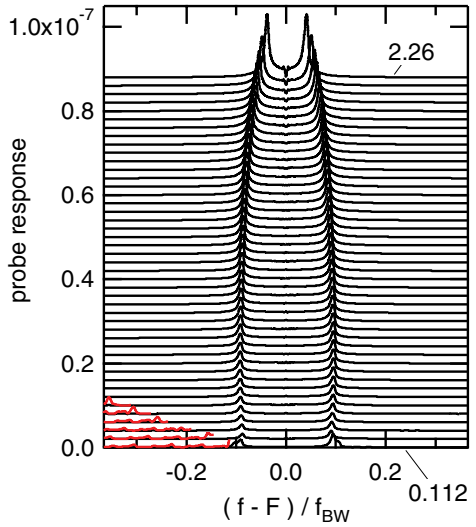

FIG. 10. (Color online) Linear response spectra of the AR state as a function of the probe frequency. These are aligned by the driver frequency from bottom to top. The entire stable frequency region of the driver frequency is shown, i.e., 137.6 to 146.4 kHz, or 0.112 to 2.26 by the normalized difference frequency $(F - f_T)/f_{\rm BW}$. The uniform probe perturbation is applied in simulations. At the upper bifurcation point, the natural resonance beat frequency softens and its peak height diverges. At the lower bifurcation point, the lower natural resonance peak overlaps with the top of the band modes, shown as small peaks near the bottom of the figure. The AR transition occurs when this linear mode overlaps via four-wave mixing. The band mode response near the lower bifurcation region are magnified 20 times. $\alpha_d = 1000$ m/s^2.

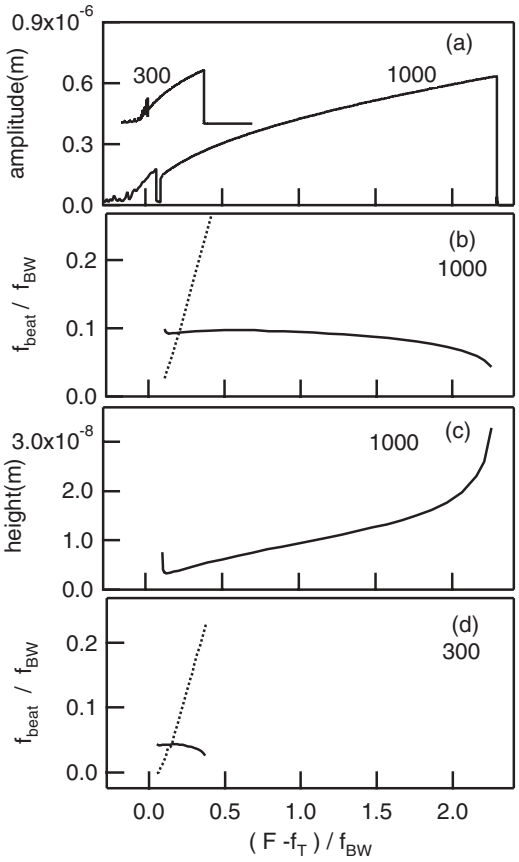

FIG. 11. (a) ILM center amplitude as a function of the driver frequency relative to the topmost band mode frequency normalized by the optical bandwidth. For $\alpha_d = 1000$ m/s^2 two different bifurcation points are identified by the sudden drops in amplitude. For $\alpha_d = 300$ m/s^2 there is no sudden drop of the amplitude at the lower AR side. (b) Normalized beat frequency between the driver and the NF (solid) and the even LLM (dashed) for $\alpha_d = 1000$ m/s^2. (c) The peak height of NF beat for the case $\alpha_d = 1000$ m/s^2. It diverges as the upper bifurcation frequency is approached. (d) NF (solid) and even LLM (dashed) beat frequencies for $\alpha_d = 300$ m/s^2. In this case, the even LLM softens before the lower NF beat intersects the top band mode at the lower bifurcation point.

sudden rise of the beat frequency and the peak height in Figs. 11(b) and 11(c) at the lower bifurcation point.]

With no clear evidence of the lower bifurcation in Fig. 11, and because of experimental evidence of the interaction between the band mode and the NF in Fig. 8, the imaginary part of linear response spectrum is plotted in Fig. 12 for all modes. Different from the spectra shown in Fig. 10, the probe perturbation is now applied to one lattice point (site 47) that is the next short cantilever site to the center of the ILM (site 49). With this one lattice point driving, all modes are excited, including the even LLM. The vibration at the perturbation site is analyzed to calculate the response spectra. The spectra are aligned from high to low normalized driver-difference frequency $(F - f_T)/f_{\rm BW}$, numbers from the top, and the spectrum at the bottom is very close to the lower bifurcation point. Initially, the even LLM is outside of the NF partner peak. When decreasing the driver frequency, this even LLM crosses the NF partner peak. Dashed curves are magnified band mode spectra that appear below the lower NF partner. The lower bifurcation point occurs when the lower NF partner coalesces with the topmost band mode.

Vibration eigenvectors of the ILM, the NF, and the even LLM are shown in Fig. 13 for two driver frequencies; one of them is very close to the lower bifurcation point and the other is very close to the upper bifurcation point. Both vibration shapes for upper and lower sideband peaks are shown. These are obtained by averaging snapshots at the maximum response instant over a few thousand periods of vibrations. Because of the cosine probe driver, the maximum response appears a quarter period delayed in each period. Only snapshots at these moments are accumulated. Again, two simulations with opposite probe phase eliminate by subtraction most of the large vibration of the ILM. The same method is used in the response calculation so the NF mixing partner labeled (NF) in Fig. 13 is upside down with respect to the NF.

When the driver frequency is large, the ILM has a large amplitude and is narrow in width. The NF has the lowest beat frequency for this case. The ILM generates at least two LLMs, the even LLM is next to the NF, and the odd LLM extends outside of the even LLM. For both even and odd shaped LLMs, the lower peaks are due to the LLMs and the upper peaks are four-wave mixing results with the ILM. The shape of the upper odd LLM is very similar to the ILM, because it is strongly affected by the shape of the ILM. When the driver frequency approaches the lower bifurcation point, i.e., the ILM becomes

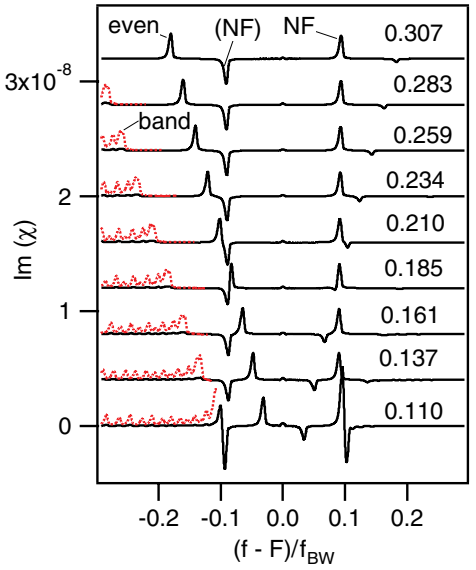

FIG. 12. (Color online) Imaginary part of the response spectra near the lower bifurcation point as a function of the probe frequency. From top to bottom, the driver frequency is decreased toward the lower bifurcation point. The lower bifurcation happens when the lower (NF) and the band mode coalesce. $\alpha_d = 1000\ \mathrm{m/s^2}$. To see all the modes, the probe perturbation is applied to a short cantilever (site 47) next to the ILM (site 49). Vibration is analyzed at the same perturbation site. Lower parts of spectra are magnified ten times to see band modes. As the lower (NF) approaches the lower bifurcation point (bottom trace), the peak heights of the (NF) and the band mode are enhanced. At the middle of this picture, the lower (NF) peak and the even LLM cross without interaction.

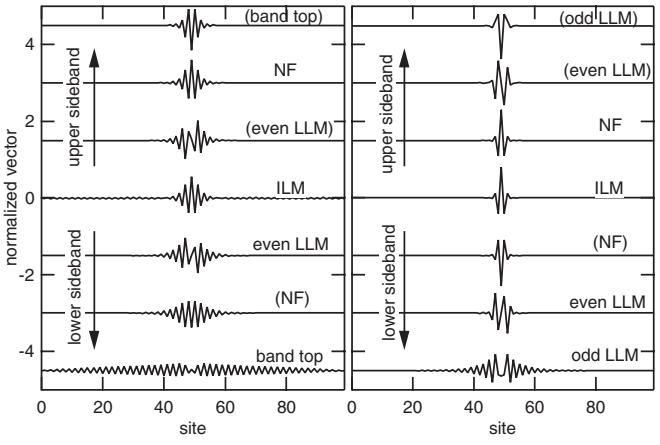

FIG. 13. Normalized vibration shapes of ILM and LLMs aligned by their peak frequencies. The left panel is for a driver frequency nearby the lower bifurcation $(F - f_T)/f_{\mathrm{BW}} = 0.137$ (137.70 kHz) and right panel is for nearby the upper bifurcation $(F - f_T)/f_{\mathrm{BW}} = 2.16$ (146.00 kHz). $\alpha_d = 1000\ \mathrm{m/s^2}$. Letters indicate names of modes, and letters with parentheses are for peaks generated by the four-wave mixing with the mode and the ILM. For the high frequency case (right), even and odd LLMs exist below the ILM. For the low frequency case (left) the odd LLM merges into the band and becomes the top band mode. In addition, the frequency of the even LLM is closer to the ILM than is the NF.

smaller and wider. The odd LLM is extended and looks like a band mode, i.e., its frequency is very close to the top of the optic band. In both frames, the NF shape is very similar to that of the ILM. On the other hand, its mixing partner labeled "(NF)" in the left panel near the lower bifurcation point is clearly different from that of NF. Since the frequency of the (NF) is very close to top of the band at the lower bifurcation, its shape is distorted by interaction with the optic band.

Another distinct feature, seen in Fig. 13, is the difference in shape between the odd-LLM (or the top band mode) at the bottom of each panel, and their mixing partner shown at the top of each panel. As shown here, the mixing partner (upper) shape now resembles the ILM. This narrower shape is generated by the nonlinear mixing the odd-LLM with the ILM, and since the ILM only exists locally the nonlinear mixing can only take place at the lattice points where the ILM exists.

VI. DISCUSSIONS

A. Upper bifurcation point for an ILM and a Duffing resonator

At the upper bifurcation of an ILM, the NF frequency approaches the driver frequency and its amplitude diverges. Simulations show good agreement with the experimental results. Clearly, the NF itself plays an important dynamic role at the upper bifurcation point. In addition the driven ILM amplitude behavior with frequency is similar to that found for the Duffing oscillator [compare Figs. 5 and 9(a)]. Also, the behavior of the ILM NF is quite similar to that found for a single Duffing oscillator, as described in Sec. II and the Appendix. At the bifurcation for both the ILM and the single Duffing resonator, as shown in Eq. (A7), the beat frequency between the driver and the NF goes to zero at the transition.

More evidence of an NF for the driven ILM is their similar shapes shown in Fig. 13. In contrast, LLMs have a completely different form than the ILM consistent with the expectation that a deformation vibration of the ILM requires the excitation of LLMs. At the same time, the similar shape in Fig. 13 means that the perturbed motion of the NF does not cause shape deformation of the driven ILM. Since there is only one degree of freedom in the single Duffing resonator, this shape resemblance between the NF and the ILM suggests the NF in both systems are similar.

To see the resemblance of the two systems more clearly, we plot the ILM center amplitude in a van der Pol plane that is usually used to analyze the Duffing oscillator [52]. Although the ILM has many degrees of freedom, only the amplitude of the center site of the ILM is monitored, because the ILM and its NF only differ in phase. To make the comparison the sine amplitude of the ILM displacement is plotted as a function of the cosine component,

$$x_i = a\cos\Omega t + b\sin\Omega t, \tag{6}$$

where x_i is the displacement at the center and a and b are cosine and sine coefficients. The results are shown in Fig. 14, where, just like Fig. 2(b), the ILM amplitude at a particular instant is described by an arrow from the origin to a point on the elliptical trajectory for a particular driving frequency and the area of the ellipse is related to the amplitude of the NF, which is driven by the weak probe. Note that at large amplitudes the major axis of the ellipse is along the θ direction of an

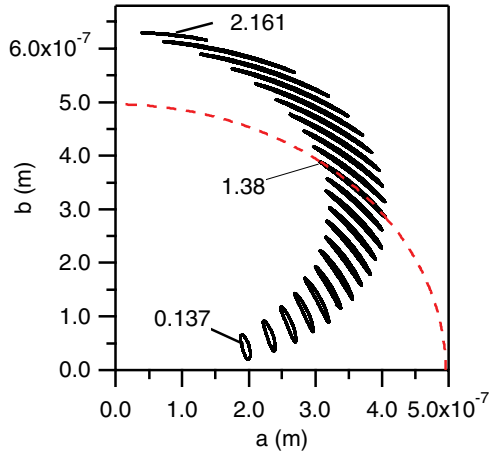

FIG. 14. (Color online) Sine coefficient b vs cosine coefficient a (van der Pol phase plane) of the probe perturbed ILM. The driver frequency is changed from $(F - f_T)/f_{BW} = 0.137$ (138 kHz) to 2.161 (146.4 kHz) with 0.098 (0.4-kHz) steps. The probe frequency is set at each NF for different driver frequencies. The stable fixed point located at each center of each ellipse moves circularly upward as the driver frequency is increased and approaches $a = 0$. The dashed curve is a quarter circle with its center at the origin. Ellipses are along the θ direction, showing that the NF causes phase oscillation of the ILM. To see these ellipses, relatively larger probe excitation amplitude 10 m/s^2 is used. The small ellipse for 2.161 is due to off resonance by the sideband response nonlinearity with the larger probe excitation amplitude.

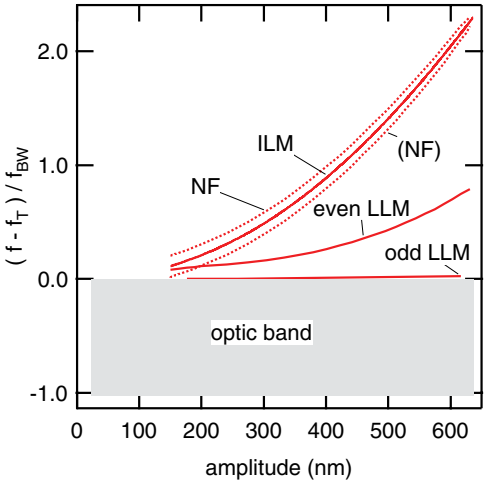

FIG. 15. (Color online) ILM, NF, even LLM, and odd LLM frequencies as a function of the ILM amplitude (frequency) for fixed $\alpha_d = 1000$ m/s^2. Lower bifurcation takes place when the lower peak of the (NF) touches the optic band. At a low driving amplitude such as $\alpha_d = 300$ m/s^2, the gap frequency of the even LLM softens before touching of the lower (NF) and the ILM begins to move laterally.

origin-centered circle (dashed curve), indicating that the NF accompanies the phase oscillation of the ILM. Our conclusion is that the dynamics of an ILM in a micromechanical array as the upper bifurcation point is approached is the same as that previously described for a single Duffing oscillator.

B. Mechanism of the lower bifurcation

The mechanism of the lower bifurcation is different from the upper one. It is related to the interaction between the NF and the band mode. This can be seen most easily by examining Fig. 15. As the ILM frequency increases with amplitude the upper and lower NF frequencies depend on the ILM amplitude, and the beat frequency softens when approaching to the upper bifurcation point. At the lower bifurcation point, the lower (NF) four-wave mixing peak intersects the band mode. Although the even LLM is very close to the driver frequency around the lower bifurcation point it does not play a role in the transition because the NF has odd symmetry.

The key to understanding the lower bifurcation is again the NF. The enhancement of the NF-response peak can be understood as follows. The NF is the positive peak on the high frequency side of the ILM. Vibration at the upper sideband peak generates a four-wave mixing signal at the lower (NF) peak. If the lower (NF) peak coalesces with the band mode frequency, the four-wave mixing signal of the upper NF resonates with it, and the resonance reduces the damping. This signal is four-wave mixed again with the large amplitude ILM and amplifies the upper NF signal. The net gain can be far larger than before coalescence and if the net gain overcomes the loss, the coupled NF and band modes grow without any driving source. Thus, the response diverges.

This process is the same as parametric oscillation by four-wave mixing, which produces two different frequencies ω_1 and ω_2 from the large amplitude vibration at Ω simultaneously when these frequencies satisfy a relation $\omega_1 + \omega_2 = 2\Omega$. A similar nonlinear process occurs in parametric oscillators and amplifiers where the three-wave mixing $\omega_1 + \omega_2 = \Omega$ process is usually employed [54,55]. Signals at ω_1 and ω_2 are called signal and idler, respectively, and some parametric oscillators have resonators to enhance the parametric process. For the ILM case, the NF can be one of the resonators and the band mode can be another resonator. Since ω_1 and ω_2 are symmetric to the driver frequency for $\omega_1 + \omega_2 = 2\Omega$, the coalescing of the lower peak of the NF and the band mode producing the idler and the resonating signal. If this process takes place, the driver energy is effectively converted into these modes, and auto oscillation will be observed producing divergence of the response peak.

A theoretical study about the lower bifurcation reveals that it is a stability transition bifurcation [22]. Before the bifurcation, there are stable ILM and low amplitude solutions. At the bifurcation, the stable ILM changes from a sink to a saddle with the remaining low amplitude stable solution. Thus, the ILM disappears and only the low amplitude state is realized [22]. From our study, the divergence of the amplitude of the NF is observed, which corresponds to the conversion of the spiral sink to a spiral source in the van der Pol phase space. The theoretical work predicts conversion to the saddle in the full phase space, while we observed switching to a source in a lower dimensional subspace of the full phase space, consistent with the theoretical work.

Figure 15 also suggests the existence of another kind of bifurcation when the even LLM softens faster than the coalescence of the band and the lower NF peak, although we have not observed such a case experimentally. We have explored

numerically the parameter space and found that such a case happens with lower driver amplitude, $\alpha_d = 300$ m/s^2. In this case, there is no low amplitude state as shown in Fig. 11(a). The ILM smoothly goes into the chaotic region when the driver frequency is decreased in simulations. The softening of the even LLM is consistent with the removal of the ILM pinning effect.

C. Application of the natural frequency measurement

There are two applications that come to mind. (1) For any driven, damped systems, the NF of a nonlinear excitation is to be expected if it has a stable fixed point in a van der Pol phase space. A four-wave emission spectrum [by Eq. (A8)] can be used to observe such an NF. For example, Kollmann *et al.* studied the stability of solitons in a discrete, driven, damped nonlinear Ablowits-Ladik Schrödinger equation [56]. Since bifurcation is realized at the edge of stable region an NF should provide a well defined marker of the incipient transition. (2) A quantum oscillator system may provide another application. There is a similar sideband structure in an emission spectrum of a driven quantum oscillator [57], indicating that the NF may exist in a quantum lattice. ILMs in quantum lattices have been studied theoretically [58–62] and experimentally [63–68]. In those systems, observation of the NF could be used to study the approach to bifurcation.

Although our linear spectroscopic measurement of the NF identifies properties near the stable point, if a barrier height can be obtained for a transition from the stable state to another stable state, it may be helpful for applications, such as exploring stochastic resonance. If the barrier height can be estimated from such a response experiment, then ILMs can be used to explore stochastic resonances, bifurcation amplifiers, or other information processing in arrays.

VII. CONCLUSION

Once the NF of a nonlinear oscillator is identified in terms of its asymptotic limit as the driver and damping simultaneously go to zero (so that its amplitude remains fixed) then the resonance plays the same role as the NF for a driven harmonic oscillator without damping. One of the main findings of this work is that this idea carries over to a discrete nonlinear lattice with many degrees of freedom. By experimental measurement and simulations it has been shown that the NF plays key, but different, roles in the two bifurcation transitions observed there. We have shown that observing the linear response spectrum via a variable frequency probe perturbation on a strongly driven nonlinear mode is very useful for experimentally studying the approach to the switching transitions. The two bifurcations of the AR-ILM observed in the cantilever array are studied both experimentally and numerically. The driver frequency is the variable parameter with which to reach the bifurcation regions that occur at both edges of the stable AR driver frequency range. The NF of the ILM is observed as a sideband pair symmetrically located about the driver frequency. Other linear features observed with this technique are an even-linear local mode and the topmost band modes. At the upper bifurcation, the NF peak approaches the driver, as measured by the softening of the beat frequency between the two. At the lower bifurcation point, the position of the four-wave mixing partner of the NF coalesces with the topmost band mode of the same symmetry and the NF amplitude diverges. The nonlinear mixing of these two modes causes auto oscillation of the NF and the ILM again becomes unstable. The tracking of the NF of the ILM is the key ingredient in identifying the approach of both transitions.

In the language of the phase space representation for this nonlinear lattice, this linear probe spectroscopy measures the local property nearby the stable ILM state as a response spectrum. For the upper bifurcation case, the saddle-node bifurcation of pair annihilation of the stable and the unstable solution causes softening of the phase oscillation in the van der Pol phase space, which is a 2D projection of the full phase space for considering the NF of the ILM. For the lower bifurcation case, it is the transition of the stable ILM solution to the saddle in this phase space. The auto oscillation of the NF indicated by the divergence of the peak amplitude is the sign of conversion from a stable sink to an unstable spiral source in the van der Pol phase plane.

ACKNOWLEDGMENTS

M.S. was supported by JSPS-Grant-in-Aid for Scientific Research No. (B) 18340086 and he thanks Dr. M. Kimura at University of Shiga Prefecture for fruitful discussions. B.E.H. and A.J.S. were supported by NSF-DMR-0906491.

APPENDIX: DRIVEN DUFFING OSCILLATOR AND ITS NATURAL FREQUENCY

Equation (1) is the model equation of the single Duffing oscillator. The driver Ω is set near its fundamental resonance and a probe (ω) spectrum response is obtained near this driver frequency. Inserting Eq. (2) into Eq. (1) and retaining terms that oscillate near the driver frequency, one finds

$$\begin{aligned}&\left(\omega_0^2+\tfrac{3}{4}\varepsilon|\tilde{A}|^2-\Omega^2-i\gamma\Omega\right)\tilde{A}e^{-i\Omega t}\\&\quad+\left(\omega_0^2+\tfrac{3}{2}\varepsilon|\tilde{A}|^2-\omega^2-i\gamma\omega\right)\tilde{a}e^{-i\omega t}+\tfrac{3}{4}\varepsilon\tilde{A}^2\tilde{b}^*e^{-i\omega t}\\&\quad+\left(\omega_0^2+\tfrac{3}{2}\varepsilon|\tilde{A}|^2-\omega'^2-i\gamma\omega'\right)\tilde{b}e^{-i\omega' t}+\tfrac{3}{4}\varepsilon\tilde{A}^2\tilde{a}^*e^{-i\omega' t}\\&=\alpha_d e^{-i\Omega t}+\alpha_p e^{-i\omega t},\end{aligned}\tag{A1}$$

where $\gamma = 1/\tau$. By equating each oscillating terms, the three resulting equations are

$$\left(\omega_0^2+\tfrac{3}{4}\varepsilon|\tilde{A}|^2-\Omega^2-i\gamma\Omega\right)\tilde{A}=\alpha_d,\tag{A2a}$$

$$\left(\omega_0^2+\tfrac{3}{2}\varepsilon|\tilde{A}|^2-\omega^2-i\gamma\omega\right)\tilde{a}+\tfrac{3}{4}\varepsilon\tilde{A}^2\tilde{b}^*=\alpha_p,\tag{A2b}$$

$$\left(\omega_0^2+\tfrac{3}{2}\varepsilon|\tilde{A}|^2-\omega'^2-i\gamma\omega'\right)\tilde{b}+\tfrac{3}{4}\varepsilon\tilde{A}^2\tilde{a}^*=0.\tag{A2c}$$

Equation (A2a) is the driver response. Where three solutions are possible for $\tilde{A}$, the high amplitude solution is taken among them. From Eqs. (A2b) and (A2c), the probe response function can be calculated as

$$\begin{aligned}\tilde{\chi}(\omega)&=\frac{\tilde{a}}{\alpha_p}\\&=\frac{1}{\left(\omega_{nl}^2-\omega^2-i\gamma\omega\right)-\frac{9}{16}\varepsilon^2|\tilde{A}|^4\frac{1}{\left(\omega_{nl}^2-\omega'^2+i\gamma\omega'\right)}}\\&=\frac{\tilde{\chi}_0(\omega)}{1-\frac{9}{16}\varepsilon^2|\tilde{A}|^4\tilde{\chi}_0(\omega)\,\tilde{\chi}_0^*(\omega')},\end{aligned}\tag{A3}$$

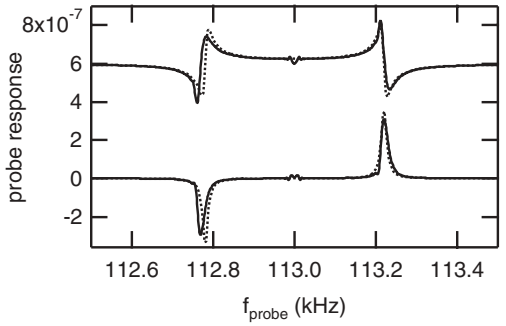

FIG. 16. Real (upper) and imaginary (lower) parts of analytical (solid) and simulated (dashed) sideband response for a single Duffing resonator as a function of probe frequency. $\alpha_d = 2000$ m/s^2 and $\alpha_p = 0.01$ m/s^2. Simulated response is obtained by eliminating the large amplitude oscillation by taking the difference of opposite probe phase simulations. The result is divided by the prove driver strength. The upper peak is larger than the lower peak and has a positive imaginary part.

where $\tilde{\chi}_0(\omega) = \frac{1}{\omega_{nl}^2 - \omega^2 - i\gamma\omega}$ and $\omega_{nl}^2 = \omega_0^2 + \frac{3}{2}\varepsilon|\tilde{A}|^2$. Real and imaginary parts of the response functions are given by $\tilde{\chi} = \chi_1 + i\chi_2$.

Note that the nonlinear frequency shift of $\tilde{a}$ and $\tilde{b}$ is twice that of $\tilde{A}$. This result is analogous to that in a nonlinear glass fiber where the phase shift due to a cross-phase modulation is twice that for self phase modulation [69]. It is this mechanism that makes the NF frequency dependence different from that of the driving frequency. It is Eq. (A2c) that brings the natural resonance close to the driver.

The solid curves in Fig. 16 show the real and imaginary parts of the analytical response curve described by Eq. (A3). Values of the parameters used throughout this Appendix are $\tau = 0.01$ s, $\omega_0 = 2\pi \times 10^5$ s^{-1}, and $\epsilon = 1.97 \times 10^{20}$ s^{-2} m^{-2}. The dashed curves in Fig. 16 show the corresponding curves by simulations. For the probe driver, we have used typically $\alpha_p = 0.01$ m/s^2. To eliminate the large amplitude vibration oscillating at the driver frequency, we made two sets of simulations with opposite probe phases, keeping the driver the same. The resultant difference between the two simulations contains only the effect of the probe. Then, the remaining displacement is multiplied by $\cos\omega t$ or $\sin\omega t$ and averaged over a certain time (like a lock-in amplifier) to obtain real and imaginary parts of the probe response. By changing the probe frequency, real and imaginary parts of the response spectra are calculated. Figure 16 shows real and imaginary parts of the probe response. The curves in Fig. 16 show good agreement between analytical solution and simulations. The small difference between them is due to scanning the probe frequency at a nonzero speed.

Similar sideband curves are obtained by Dykman *et al.* in Refs. [46,70]. They studied the Duffing oscillator as a foundation for a stochastic resonance situation. Since noise plays an important role in the stochastic resonance, they calculated a spectral density of vibration analytically (Eq. (19) in Ref. [46]). Although their equation is somewhat more complex than ours, it reproduces our sideband curve, the beat frequency, and peak height well if we calculate the spectral density of only the high amplitude state ($j = 3$ in their notation) in their Eq. (19).

The beat frequency ω_b is calculated from the denominator of Eq. (A3) by setting its real part to zero, ignoring the damping γ. The result is

$$\omega_b = \omega_n - \Omega = \sqrt{\Omega^2 + \omega_{nl}^2 - \sqrt{4\Omega^2\omega_{nl}^2 + \tfrac{9}{16}\varepsilon^2|\tilde{A}|^4}}. \quad \text{(A4)}$$

The beat frequency is related to the stability of the stationary state. For the Duffing equation, the stability can be checked by evaluating perturbed equations at the stationary state [Chap. 4.1 in Ref. [71], or Chap. 7 in Ref. [72]]. For example, from the equation of motions for $a(t)$ and $b(t)$ (Eqs. (7.16) and (7.17) in Ref. [72]) and their linear approximated equations (Eq. (7.21) in Ref. [72]), one can obtain a second order

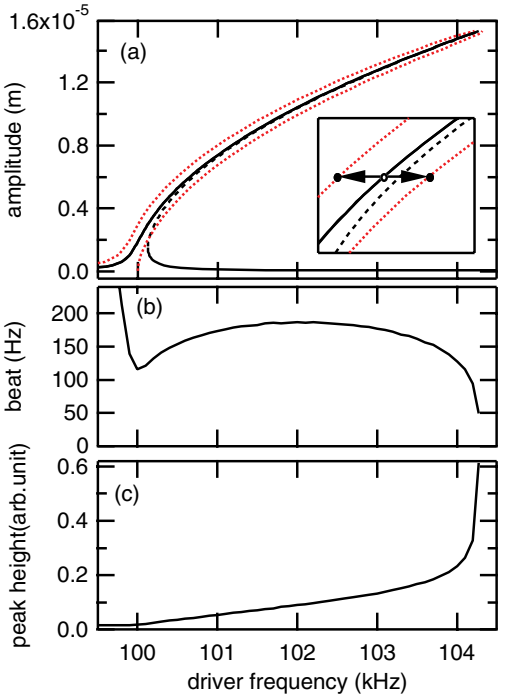

FIG. 17. (Color online) (a) The driver response and the NF as a function of the driver frequency of the Duffing resonator. $\alpha_d = 1000$ m/s^2. Solid curve is the stable driver response amplitude, and long dashed curve is the unstable branch. Dotted curve is the natural resonance curve for the high amplitude solution. Inset is the magnified picture at a middle range, it shows how to find the natural frequency. For a given driver frequency, find a point (open circle) on the driver response curve indicated by the solid curve. Draw a horizontal line and find crossing points with the dotted curves. These points indicate the natural frequency at the amplitude determined by the driver frequency. As the amplitude decreasing, the upper natural frequency peak is approaching the linear resonance peak. When the driver frequency is nearby the linear resonance frequency, the lower peak is very small and the upper peak is dominant. Note that the position of the natural frequency peak is different from the unstable solution. (b) The beat frequency of the natural frequency as a function of the driver frequency. It goes to zero as approaching to the upper bifurcation. (c) The peak height of the natural frequency as a function of the driver frequency. It diverges at the upper bifurcation point.

derivative equation with one variable by inserting one of the linearized equations. The oscillation frequency can be calculated as

$$\omega_b^2 = \frac{1}{4\Omega^2}\left[\left(\omega_{nl}^2 - \Omega^2\right)^2 - \varepsilon^2\frac{9}{16}|\tilde{A}|^4\right]. \tag{A5}$$

The beat frequency by Eq. (A4) can be approximated to Eq. (A5) by using the fact $\omega_b \ll \Omega, \omega_{nl}$. There is not much difference in the driver frequency dependence of the beat frequency between these two equations.

The single Duffing resonator has one bifurcation point with increasing frequency for the AR high amplitude state, where the amplitude drops suddenly. The beat frequency by Eq. (A5) decreases as it is approached. The bifurcation frequency is calculated from Eq. (A2a) as

$$\Omega = \sqrt{\omega_0^2 + \frac{3}{4}\varepsilon|\tilde{A}|^2 - \frac{\gamma^2}{2}} \approx \sqrt{\omega_0^2 + \frac{3}{4}\varepsilon|\tilde{A}|^2}. \tag{A6}$$

Inserting this result into Eq. (A5) gives zero frequency, so

$$\omega_b^2 = \frac{1}{4\Omega^2}\left[\left(\omega_0^2 + \frac{3}{2}\varepsilon|\tilde{A}|^2 - \omega_0^2 - \frac{3}{4}\varepsilon|\tilde{A}|^2\right)^2 - \varepsilon^2\frac{9}{16}|\tilde{A}|^4\right] = 0. \tag{A7}$$

Figure 17 shows the natural resonance frequency as a function of the driver frequency. Solid and long dashed curves in Fig. 17(a) are the stable and unstable solutions, respectively. Dotted curves are upper and lower natural resonance frequencies, as a function of the amplitude. To find those frequencies, determine the amplitude at a given driver frequency first (open circle). Then, draw a horizontal line. See two crossing points with the dotted curves (solid circles). These frequencies are the natural resonance frequencies. Figure 17(b) is the beat frequency. It increases first, then goes to zero at the upper bifurcation point. Figure 17(c) is the peak height. It gradually increases at lower frequency, but diverges at the bifurcation point.

Although Eq. (A3) gives the response for the high amplitude state, it can be applied to the low amplitude state by using the low amplitude solution among three solutions of $\tilde{A}$. In this case there is only one resonance peak below the driver frequency, nearby the linear resonance frequency. Because of the low amplitude of the driver response, and because of weak four-wave mixing process, the other peak is not seen in the spectrum. As the driver frequency decreases approaching a low to high bifurcation point, the NF peak approaches the driver frequency and the amplitude jumps to high amplitude [36,48].

In addition, the four-wave emission spectrum can be calculated from Eq. (A2) as follows:

$$\tilde{\chi}_{\text{emission}}(\omega) = \frac{\tilde{b}}{\alpha_p} = -\frac{3}{4}\varepsilon\tilde{A}^2\tilde{\chi}(\omega')\frac{\tilde{a}^*}{\alpha_p} = \frac{-\frac{3}{4}\varepsilon\tilde{A}^2\tilde{\chi}(\omega')\tilde{\chi}_0^*(\omega)}{1 - \frac{9}{16}\varepsilon^2|\tilde{A}|^4\tilde{\chi}_0^*(\omega)\tilde{\chi}_0(\omega')}. \tag{A8}$$

Because of very similar denominator of Eq. (A8) to Eq. (A3), the emission spectrum has the same two peak structure as the response function when the amplitude $|\tilde{A}|$ is large. Such sidebands have been observed in a four-wave emission spectrum of the driven antiferromagnet, $C_2H_5CH_3(CuCl_4)_2$ [66,73].

[1] A. S. Dogolov, Sov. Phys. Solid State **28**, 907 (1986).
[2] A. J. Sievers and S. Takeno, Phys. Rev. Lett. **61**, 970 (1988).
[3] J. B. Page, Phys. Rev. B **41**, 7835 (1990).
[4] S. Takeno and A. J. Sievers, Solid State Commun. **67**, 1023 (1988).
[5] A. J. Sievers and J. B. Page, *Dynamical Properties of Solids: Phonon Physics the Cutting Edge* (North Holland, Amsterdam, 1995), p. 137.
[6] S. Flach and C. R. Willis, Phys. Rep. **295**, 182 (1998).
[7] D. K. Campbell, S. Flach, and Y. S. Kivshar, Phys. Today **57**, 43 (2004).
[8] S. Flach and A. Gorbach, Phys. Rep. **467**, 1 (2008).
[9] B. A. Malomed, Phys. Rev. A **45**, 4097 (1992).
[10] S. A. Kiselev, S. R. Bickham, and A. J. Sievers, Phys. Rev. B **48**, 13508 (1993).
[11] T. Rössler and J. B. Page, Phys. Lett. A **204**, 418 (1995).
[12] R. Lai and A. J. Sievers, Phys. Rep. **314**, 147 (1999).
[13] M. Sato, B. E. Hubbard, A. J. Sievers, B. Ilic, D. A. Czaplewski, and H. G. Craighead, Phys. Rev. Lett. **90**, 044102 (2003).
[14] M. Sato, B. E. Hubbard, and A. J. Sievers, Rev. Mod. Phys. **78**, 137 (2006).
[15] V. Hizhnyakov, A. Shelkan, M. Klopov, S. A. Kiselev, and A. J. Sievers, Phys. Rev. B **73**, 224302 (2006).
[16] E. Kenig, B. A. Malomed, M. C. Cross, and R. Lifshitz, Phys. Rev. E **80**, 046202 (2009).
[17] Y. Doi and K. Yoshimura, J. Phys. Soc. Jpn. **78**, 034401 (2009).
[18] E. Kenig, R. Lifshitz, and M. C. Cross, Phys. Rev. E **79**, 026203 (2009).
[19] P. Maniadis and S. Flach, Europhys. Lett. **74**, 452 (2006).
[20] M. Spletzer, A. Raman, A. Q. Wu, and X. Xu, Appl. Phys. Lett. **88**, 254102 (2006).
[21] A. J. Dick, A. J. Balachandran, and C. D. Mote, Nonlin. Dyn. **54**, 13 (2008).
[22] Q. Chen, Y.-C. L. L. Huang, and D. Dietz, Chaos **19**, 013127 (2009).
[23] J. Wiersig, S. Flach, and K. H. Ahn, Appl. Phys. Lett. **93**, 222110 (2009).
[24] M. Kimura and T. Hikihara, Chaos **19**, 013138 (2009).
[25] L. Q. English, F. Palmero, A. J. Sievers, P. G. Kevrekidis, and D. H. Barnak, Phys. Rev. E **81**, 046605 (2010).
[26] M. Sato, S. Imai, N. Fujita, S. Nishimura, Y. Takao, Y. Sada, B. E. Hubbard, B. Ilic, and A. J. Sievers, Phys. Rev. Lett. **107**, 234101 (2011).
[27] Y. Doi and A. Nakatani, J. Solid Mech. Mater. Eng. **6**, 71 (2012).
[28] Y. Watanabe, K. Hamada, and N. Sugimoto, J. Phys. Soc. Jpn **81**, 014002 (2012).
[29] M. Sato, B. E. Hubbard, L. Q. English, B. Ilic, D. A. Czaplewski, H. G. Craighead, and A. J. Sievers, Chaos **13**, 702 (2003).

[30] J. Fajans, E. Gilson, and L. Friedland, Phys. Plasmas **6**, 4497 (1999).
[31] J. Fajans and L. Friedland, Am. J. Phys. **69**, 1096 (2001).
[32] S. V. Batalov and A. G. Shagalov, Phys. Rev. E **84**, 016603 (2011).
[33] Y. Gopher, L. Friedland, and A. G. Shagalov, Phys. Rev. E **72**, 036604 (2005).
[34] A. Barak, Y. Lamhot, L. Friedland, and M. Segev, Phys. Rev. Lett. **103**, 123901 (2009).
[35] O. Naaman, J. Aumentado, L. Friedland, J. S. Wurtele, and I. Siddiqi, Phys. Rev. Lett. **101**, 117005 (2008).
[36] J. M. T. Thompson and H. B. Stewart, *Nonlinear Dynamics and Chaos* (Wiley & Sons, Chichester, 1986).
[37] I. Serban, M. I. Dykman, and F. K. Wilhelm, Phys. Rev. A **81**, 022305 (2010).
[38] A. Chatterjee, Int. J. Mech. Sci. **52**, 1716 (2010).
[39] A. Elias-Zuniga, Nonlin. Dyn. **45**, 227 (2006).
[40] B. Yurke, D. S. Greywall, A. N. Pargellis, and P. A. Busch, Phys. Rev. A **51**, 4211 (1995).
[41] A. G. Shagalov, J. J. Ramsmussen, and V. Naulin, J. Phys. A: Math. Theor. **42**, 045502 (2009).
[42] K. M. Murch, R. Vijay, I. Barth, J. A. Aumentado, L. Friedland, and I. Siddiqi, Nat. Phys. **7**, 105 (2011).
[43] R. B. Karabalin, R. Lifshitz, M. C. Cross, M. H. Matheny, S. C. Masmanidis, and M. L. Roukes, Phys. Rev. Lett. **106**, 094102 (2011).
[44] I. Kozinsky, H. W. C. Postma, O. Kogan, A. Husain, and M. L. Roukes, Phys. Rev. Lett. **99**, 207201 (2007).
[45] J. S. Aldridge and A. N. Cleland, Phys. Rev. Lett. **94**, 156403 (2005).
[46] M. I. Dykman, D. G. Luchinsky, R. Mannella, P. V. E. McClintock, N. D. Stein, and N. G. Stocks, Phys. Rev. E **49**, 1198 (1994).
[47] H. B. Chan and C. Stambaugh, J. Stat. Mech.: Theory Exp. (2009) P01028.
[48] J. M. T. Thompson and L. N. Virgin, Int. J. Nonlinear Mech. **21**, 205 (1986).
[49] V. Hizhnyakov, A. Shelkan, M. Klopov, and A. J. Sievers, J. Lumin. **128**, 995 (2008).
[50] L. D. Landau and E. M. Lifshitz, *Mechanics* (Pergamon Press, Oxford, 1960).
[51] S. M. Soskin, R. Mannella, and P. V. E. McClintock, Phys. Rep. **373**, 247 (2003).
[52] D. W. Jordan and P. Smith, *Nonlinear Ordinary Differential Equations* (Oxford University Press, New York, 2007).
[53] Q. F. Chen, L. Huang, and Y. C. Lai, Appl. Phys. Lett. **92**, 241914 (2008).
[54] R. G. Smith, in *Laser Handbook*, edited by F. T. Arecchi and E. Q. Schulz-Dubois (North Holland, Amsterdam, 1972), Vol. 1.
[55] Y. R. Shen, *The Principles of Nonlinear Optics* (Wiley & Sons, New York, 1984).
[56] M. Kollmann, H. W. Capel, and T. Bountis, Phys. Rev. E **60**, 1195 (1999).
[57] S. André, L. Guo, V. Peano, M. Marthaler, and G. Schon, Phys. Rev. A **85**, 053825 (2012).
[58] T. Rössler and J. B. Page, Phys. Rev. B **51**, 11382 (1995).
[59] S. Aubry, Physica D **103**, 201 (1997).
[60] S. Takeno, M. Kubota, and K. Kawasaki, Physica D **113**, 366 (1998).
[61] V. Hizhnyakov, D. Nevedrov, and A. J. Sievers, Physics B **316-317**, 132 (2002).
[62] P. S. Riseborough, Phys. Rev. E **85**, 011129 (2012).
[63] B. I. Swanson, J. A. Brozik, S. P. Love, G. F. Strouse, A. P. Shreve, A. R. Bishop, W.-Z. Wang, and M. I. Salkola, Phys. Rev. Lett. **82**, 3288 (1999).
[64] E. Trías, J. J. Mazo, and T. P. Orlando, Phys. Rev. Lett. **84**, 741 (2000).
[65] A. V. Ustinov, Chaos **13**, 716 (2003).
[66] M. Sato and A. J. Sievers, Nature (London) **432**, 486 (2004).
[67] B. Eiermann, T. Anker, M. Albiez, M. Taglieber, P. Treutlein, K.-P. Marzlin, and M. K. Oberthaler, Phys. Rev. Lett. **92**, 230401 (2004).
[68] M. E. Manley, A. J. Sievers, J. W. Lynn, S. A. Kiselev, N. I. Agladze, Y. Chen, A. Llobet, and A. Alatas, Phys. Rev. B **79**, 134304 (2009).
[69] G. P. Agrawal, *Nonlinear Fiber Optics* (Academic Press, San Diego, 1989).
[70] D. G. Luchinsky, P. V. E. McClintock, and M. I. Dykman, Rep. Prog. Phys. **61**, 889 (1998).
[71] A. H. Nayfeh and D. T. Mook, *Nonlinear Oscillations* (Wiley & Sons, New York, 1995).
[72] D. W. Jordan and P. Smith, *Nonlinear Ordinary Differential Equations* (Oxford University Press, Oxford, 1999).
[73] M. Sato and A. J. Sievers, Phys. Rev. B **71**, 214306 (2005).